Semi-batch photocatalytic reduction of nitrates:

Role of process conditions and co-catalysts

Elnaz Bahadori[a], Antonio Tripodi[b], Gianguido Ramis[a], Ilenia Rossetti[b,*]

[a] Dip. Ing. Chimica, Civile ed Ambientale, Università degli Studi di Genova and INSTM Unit Genova, via all'Opera Pia 15A, 16145 Genoa, Italy

[b] Chemical Plants and Industrial Chemistry Group, Dip. Chimica, Università degli Studi di Milano, CNR-ISTM and INSTM Unit Milano-Università, via C. Golgi 19, 20133 Milan, Italy

Abstract

Photocatalysis has been used to reduce nitrate ions from waste and drinking water. A semibatch photoreactor was developed for this process and commercial nanostructured TiO_2 (P25) and TiO_2 in nanosized form prepared by flame spray pyrolysis (FSP) were used as catalysts. Several noble metals were added as co-catalyst on both titania samples and the chemical physical properties of every sample were studied by XRD, BET and UV-Vis spectroscopy techniques. The optimum pH to reach the highest conversion of nitrates with lower selectivity toward ammonia was different for P25 and FSP samples, at basic pH and nearly neutral, respectively.

The bare and doped FSP samples, with higher surface area, showed higher nitrates conversion with respect to P25-based samples. The photocatalytic rate of nitrate reduction over undoped TiO_2 was higher than that of most noble metal loaded TiO_2, except Ag. The highest activity for nitrate

* Corresponding author: Fax: +390250314300; email ilenia.rossetti@unimi.it.

conversion has been obtained by adding Ag on P25 and FSP, increasing the conversion up to 3.5 and 1.5 times with respect to the bare semiconductor, respectively.

Keywords: Nitrates reduction; Photocatalysis; TiO_2; Wastewater treatment; Photocatalytic reduction.

1. Introduction

Essential for life, clean water is one of the most important natural resources on the planet. Wastewater becomes a valuable resource, especially with recurring droughts and water shortages in many areas of the world. However, wastewater contains many harmful substances and cannot be released back into the environment until it is treated. Thus, the importance of wastewater treatment is twofold: to restore the water supply and to protect the environment from harmful compounds.

Nitrogen containing compounds are among the most abundant water pollutant. They are toxic to humans and, in combination with P-containing compounds, are the main reason of eutrophication (hypertrophication) of the environment [1,2]. The main possible sources of N-containing pollutants are: *i*) nature; *ii*) industrial effluents [3] and inputs from agricultural runoff [4–6] *iii*) pharmaceuticals and cosmeceutical products (PPCPs) [7]; *iv*) disinfection by-products (DBPs) [8].

The major sources of nitrogen to rivers include runoff and leaching in non-cultivated areas, the diffusion of excess nitrogen added to soils and urban or industrial wastewater treatment plants, which often do not include a tertiary post-treatment of denitrification. According to statistical estimation of organization for Economic Co-operation and Development [9] around 70% of the nitrogen content in rivers reaches coastal waters, while 30% is retained in groundwater, the main

nitrogen compound being nitrate (NO_3^-) with a half-life of two to three years. There are several available techniques for wastewater treatment (*e.g.* physical, biological and chemical), which can be standalone methods, or to be optimized by their combination [10,11].

Physical methods (*e.g.* adsorption/coagulation, sedimentation, filtration and membrane technologies) with aim of collecting and transferring the pollutant from water to another phase, may generate secondary pollutants successively released in the ecosystem and have high operating costs [12]. Currently, biological methods with high flexibility and low cost are the most common at industrial scale. However, they are time consuming, intolerant to high concentration and ineffective for a variety of recalcitrant (hardly biodegradable) pollutants, needing pre/post-treatments [10,13]. Chemical methods (*e.g.* chlorination) may generate mutagenic and/or carcinogenic DBPs [14].

Advanced oxidation processes (AOPs) [15] represent innovative technologies for wastewater treatment by formation of highly reactive transient species (*e.g.* OH•, H_2O_2, $O_2^{\bullet -}$, O_3), which in turn can enhance the mineralization of non-biodegradable organic compounds and side DBPs into carbon dioxide, water and a mineral acid [16] (Table 1). Among them the ones based on photochemical or photocatalytic routes are becoming more and more important.

Table 1: Some common AOPs [17]

Non photochemical AOPs	**Photochemical AOPs**
Ozone (O_3)	Photolysis (UV + H_2O_2)
Fenton (Fe^{2+} + H_2O_2)	Photocatalysis (light + catalysis)
Electrolysis (electrodes + current)	Photo-Fenton (solar light + Fenton)
Sonolysis (ultrasound)	
Microwaves + H_2O_2	

The photocatalytic treatments can be equally applied also to reduction processes, such as denitrification, whose objective is the photoreduction of nitrate to innocuous nitrogen gas through the action of a photocatalyst [18–21]. These may represent an economically viable solution with environmental benefits compared to other treatments available for the removal of nitrogen from aqueous media.

Several semiconducting catalysts can be used for the photocatalytic reduction (*e.g.* TiO_2, Fe_2O_3, ZnO, CdS, GaP, ZnS) [22], among which TiO_2 is the most commonly studied and low cost photocatalysts with high accessibility, stability, recyclability, environmental sustainability and activity for degradation of the pollutants under UV light [22–27]. Irradiation (energy $_{light} \geq$ band gap energy) produces photogenerated electron/hole (e^-/h^+) pairs that are charge carriers and can promote reduction and oxidation reactions (Table 2; eq. 1-7) with compounds either adsorbed on or in proximity of the TiO_2 surface.

The modification of TiO_2 structure either by different synthesis techniques and changing the crystalline phases [28,29] or the addition of either metal or non-metal elements have been proposed as strategies to improve the photocatalytic activity and to enhance light harvesting. Co-catalysts, such as Pd, Pt, Au and Cu usually improve the photocatalytic activity of TiO_2 either by reducing the band gap and shifting light harvesting towards the visible part of the spectrum, with the ultimate goal of using solar radiation [23,24,30,31] and/or enhancing charge separation by easing the charge-transfer between the metal and the semiconductor [32,33]. Meanwhile, noble metals, such as Au and Ag nanoparticles exhibit higher light absorption due to resonance between the incident electromagnetic wave and the collective motion of conduction (free) electrons at metal surfaces, called localized surface plasmon resonance (LSPR), which is advantageous to absorb white light [34,35]. The SPR peak wavelength is affected not only on metal species but also on their size. For

instance, the LSPR peak of spherical gold nanoparticles is present at ca. 520 nm, and for gold nanorods, at ca. 510 nm (transverse mode) and other forms at a longer wavelength [36,37]. Whereas, for spherical silver nanoparticles, the SPR band is located at a shorter wavelength (390 nm) but with higher intensity with respect to gold [36,37]. In the present case the mechanism of degradation is more complex, since different consecutive reduction products are possible: NO_2^- (nitrite), N_2, which is the desired product, and NH_3/NH_4^+ (Scheme 1) [38]. Both NO_2^- and NH_3 are harmful products, so their selectivity should be minimised.

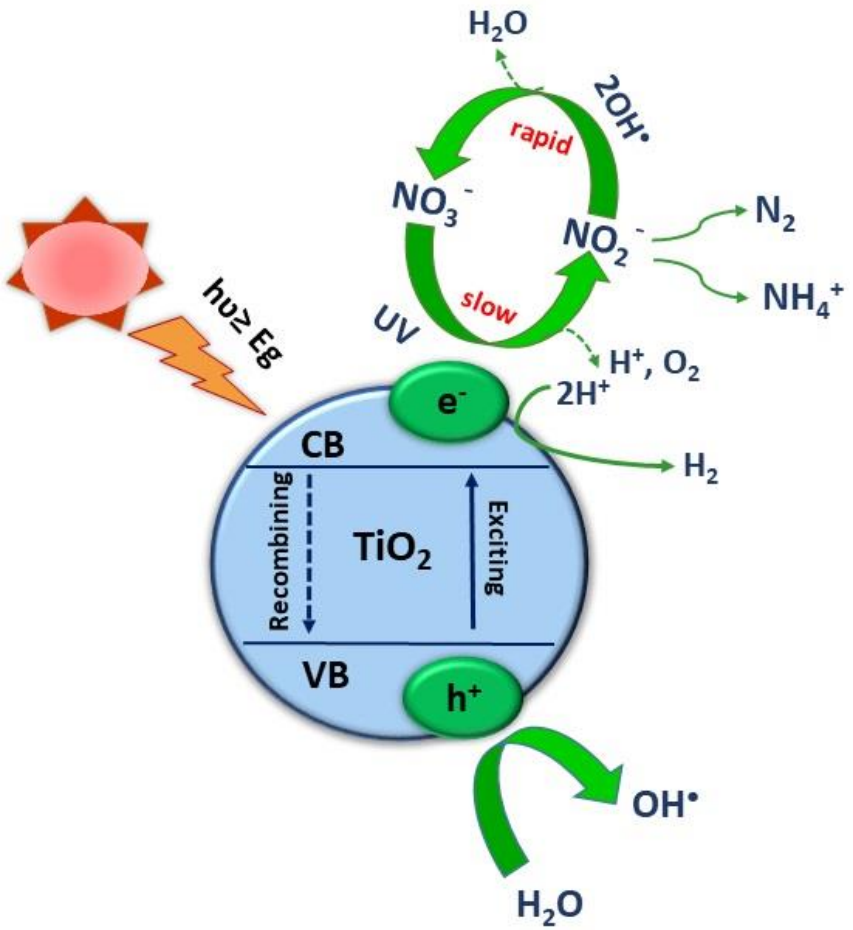

Scheme 1: Mechanism of photoreduction of Nitrates

The reduction of NO^{3-} and NO^{2-} through catalytic, electrocatalytic and photocatalytic processes has been studied, however, the over-reduction to NH_3/NH^{4+} and, thus, minor selectivity toward N_2 still remains the main issue (Table 2) [23,39,40].

The aim of this work is to investigate the mechanism, conversion and selectivity of different photocatalysts for the photoreduction of nitrates. For this purpose, commercial TiO_2 (Evonink P25) and TiO_2 obtained by Flame Spray Pyrolysis (FSP), either as such or with different metal co-catalysts (0.1 mol % Ag, Au, Pd and Pt, loaded by impregnation) and the optimum pH condition for nitrate conversion have been investigated. Finally, the conversion and selectivity toward different products have been studied.

Table 2: Expected reactions in nitrates photoreduction

	Equation no.	Equation	Rate Constant	pKa	Ref
Reactions	1	$TiO_2 + h\upsilon \rightarrow TiO_2 + {e_{CB}}^- + {h_{VB}}^+$			
	2	$H_2O + {h_{VB}}^+ \rightarrow H^+ + OH^\bullet$			
	3	$(O_2)_{ads} + {e_{CB}}^- \rightarrow {O_2}^{\bullet-}$			
	4	$2H^+ + 2e^- \rightarrow H_2$			
	5	$R^\bullet + H^+ \rightarrow RH^{\bullet+} \rightarrow intermediates/final\ products$			
	6	${O_2}^{\bullet-} + H^+ \rightarrow {HO_2}^\bullet$			
	7	${HO_2}^\bullet + {e_{CB}}^- \rightarrow {HO_2}^-$			
NO_3^- reduction	8	${NO_3}^- + h\upsilon \leftrightarrow {NO_2}^\bullet + O^{\bullet-}$			[41]
	9	${NO_3}^- + h\upsilon \leftrightarrow ONOO^-$			[41]
	10	$ONOO^- + h\upsilon \leftrightarrow NO^\bullet + {O_2}^{\bullet-}$			[41]
	11	$NO^\bullet + OH^\bullet \leftrightarrow HNO_2$	8.9×10^9 ($\frac{1}{M.s}$) (T=25°C)		[41]
	12	${NO_3}^- + 10H^+ + 8e^- \leftrightarrow {NH_4}^+ + 3H_2O$			[42]
	13	$2{NO_3}^- + 10H^+ + 8e^- \rightarrow N_2O + 5H_2O$			[42]
	14	${NO_3}^- + 2H^+ + 2e^- \rightarrow {NO_2}^- + H_2O$			[42]
	15	${NO_3}^- + H_2O + 2e^- \rightarrow {NO_2}^- + 2OH^-$	5.5×10^4 ($\frac{1}{s}$)		[43]
	16	$2{NO_3}^- + 12H^+ + 10e^- \rightarrow N_2 + 6H_2O$			
	17	${NO_3}^- + e^- \rightarrow {NO_3}^{2-}$		3.3	[42]
NO_2^- reduction	18	${NO_2}^- + 8H^+ + 6e^- \leftrightarrow {NH_4}^+ + 2H_2O$			
	19	$2{NO_2}^- + 8H^+ + 6e^- \rightarrow N_2 + 4H_2O$			
	20	$5{NO_2}^- + 2H^+ \rightarrow N_2 + 3{NO_3}^- + H_2O$			[44]
	21	$2HNO_2 \leftrightarrow NO + NO_2 + H_2O$	13.4×10^8 ($\frac{1}{M.s}$) (T=22 °C)		[45]
NO_2^- oxidation	22	${NO_2}^- + OH^\bullet \rightarrow {NO_2}^\bullet + OH^-$	1.1×10^{10} ($\frac{1}{M.s}$) (T=25°C)		[46]
	23	${NO_2}^\bullet + OH^\bullet \rightarrow {NO_3}^- + H^+$	1×10^{10} ($\frac{1}{M.s}$) (T=25°C)		[47]
	24	$2{NO_2}^\bullet + H_2O \rightarrow {NO_2}^- + {NO_3}^- + H^+$	6.5×10^7 ($\frac{1}{M.s}$) (T=25°C)		[41]
	25	$3{NO_2}^- + 3H_2O + 6h^+ \rightarrow 3{NO_3}^- + 6H^+$			

2. Experimental

2.1. Materials Preparation

TiO_2-FSP samples were prepared using a home-developed device [48,49], composed of a burner which feeds simultaneously the titania precursor solution and 5 L/min of oxygen. The flame is ignited by a ring of flamelets (0.5 L/min CH_4 + 1 L/min of O_2). The oxide precursor solution, prepared with an organic solvent, is continuously fed to the burner through a syringe pump with the rate of 2.5 mL/min. Titanium isopropoxide (Sigma Aldrich, pur. 97%) as TiO_2 precursor was dissolved in o-xylene and propionic acid (Sigma Aldrich, pur. 97%) with a 0.4 M concentration and injected through the burner. The pressure drop at the burner nozzle was 1.5 bar.

Different precursors have been used to add 0.1 mol% of Au, Ag, Pd and Pt and Ag on both P25 and FSP samples by impregnation. The details on reagents and method of loading have been summarized in Table 3.

The metals reduction was obtained by heating 10 °C/min in H_2 flow at different temperatures for 3h, according to preliminary Temperature Programmed Reduction (TPR) (Table 3).

Table 3: Precursors and reduction temperature for addition of metals on titanium dioxide (P25, FSP).

Acac = acetylacetonate.

Catalyst name	**Co-Catalysts (mol%)**	**Precursor**	**Reduction T (˚C)**
Au-P25 / Au-FSP	Au (0.1%)	$NaAuCl_4 \cdot 2H_2O$	700
Ag –P25 / Ag-FSP	Ag (0.1%)	$AgNO_3$	150
Pd –P25 / Pd-FSP	Pd (0.1%)	$Pd(NO_3)_2 \cdot xH_2O$	300
Pt-P25 / Pt-FSP	Pt (0.1%)	$Pt(acac)_2$	700

2.2. Materials characterization

X-ray diffraction (XRD) analysis was performed with a Philips 3020 instrument using the Cu-Kα (λ = 1.5406 Å) radiation, with a graphite monochromator on the diffracted beam. Data were collected in the 20° – 90° 2θ range with 0.03° step size and 4 s step time. The voltage and current intensity of the generator were set at 40 kV and 30 mA respectively.

N_2 adsorption and desorption isotherms were collected with a Micromeritics ASAP2020 apparatus. To determine BET SSA (Brunauer-Emmett-Teller Specific Surface Area) and porous volume, N_2 isotherms were measured at -196 ˚C on samples previously outgassed at 150 ˚C overnight. Micropores volume was calculated according to the t-plot method.

Diffuse Reflectance (DR) UV-Vis spectra of samples were measured on a Cary 5000 UV-Vis-NIR spectrophotometer (Varian instruments) in the range of 200–800 nm.

TPR analysis was carried out on a bench scale apparatus by flowing 40 mL/min of a 10 vol% H_2/N_2 mixture, while heating the sample by 10 °C/min up to 800°C. The gas outflowing the quartz reactor was analyzed by with a TCD detector after entrapping the possibly formed water through a cold trap.

2.3. Photoreactor and testing condition

The experimental apparatus consists of the cylindrical photoreactor with cooling jacket through continuosly flowing water. It has a total volume of *ca*. 300 mL, holding 250 mL of solution and is irradiated with a cylindrical, coaxial submerged lamp. A medium-pressure Hg vapour lamp (200 W UVA; Jelosil HG 200 L) with maximum emission at 365 nm has been selected as an irradiation source. Lamp power has been obtained using a photoradiometer (delta OHM HD2102,2). The test was performed in the middle of the bulb and shows an average irradiance of 60 W/m^2.

The reactor includes inlets directly connected to the helium line for degassing, outlets for liquid phase sampling and a second one for gas output, which is directly connected to a gas chromatograph (HP 5890 Series II) for gas phase analysis.

For each experiment, 250 mL of a 6 mM $NaNO_3$ solution has been prepared and loaded in the reactor. 250 mg of catalyst (1-1.25 g/L) have been suspended by magnetic agitation. The system is outgassed for 100 min by flowing He (95 mL/min), which is also continuously fed during the whole test (semi-batch mode). After switching on the lamp, sampling of both the liquid and the gas phases have been carried out every hour for total reaction time of 5 h.

An Ion Chromatograph (Metrohm, 883 Basic IC Plus) has been used for quantification of nitrite and nitrate ions, while the indophenol standard method has been used for quantification of ammonia by UV-Vis spectroscopy (Perkin Elmer Lambda 35). N_2 can be analyzed in line by sampling the continuous He flow in a gas chromatograph (HP 5890). The results were significant only for high nitrate conversion and initial concentration, for which N_2 concentration was analysed and was demonstrated to close the N-balance. This allowed to exclude the presence of undetectable intermediates or co-products: the only observed products were NO_2^-, N_2 and NH_3/NH_4^+. At low nitrate concentration the N_2 concentration was too low to be significant over the background of the photoreactor. Thus, for the sensitivity of the analysis, selectivities (when relevant) are reported only for ammonia and nitrites.

3. Results and Discussion

3.1. Powders characterization

The XRD pattern of all samples shows a mixture of the crystalline phases of anatase and rutile. All the reflections were identified by comparison with the standard JCPDS data of rutile (file 88-

1175) and anatase (file 84-1286) [50]. Both metal loaded samples and bare TiO_2 have the same XRD pattern and no extra reflection has been observed in the XRD pattern of metal loaded samples. This result was expected due to the very low metal amount, but it also testifies that such a low metal loading, in high dispersion, does not affect the crystalline structure of TiO_2.

The phase composition of each sample has been determined from the intensity ratio between the reflections of anatase (101) and (110) rutile planes, respectively [51]. The average particle size was determined from the broadening of the (101) peak at ($2\theta = 25.3°$) and has been calculated using the Scherrer equation [52]. The rutile percentage in FSP samples was slightly higher than P25. The FSP samples also showed bigger crystal size with respect to P25 samples. The XRD pattern of bare P25 and FSP samples are reported in Figure 1 and the data of phase composition and crystal size from XRD are reported in Table 4.

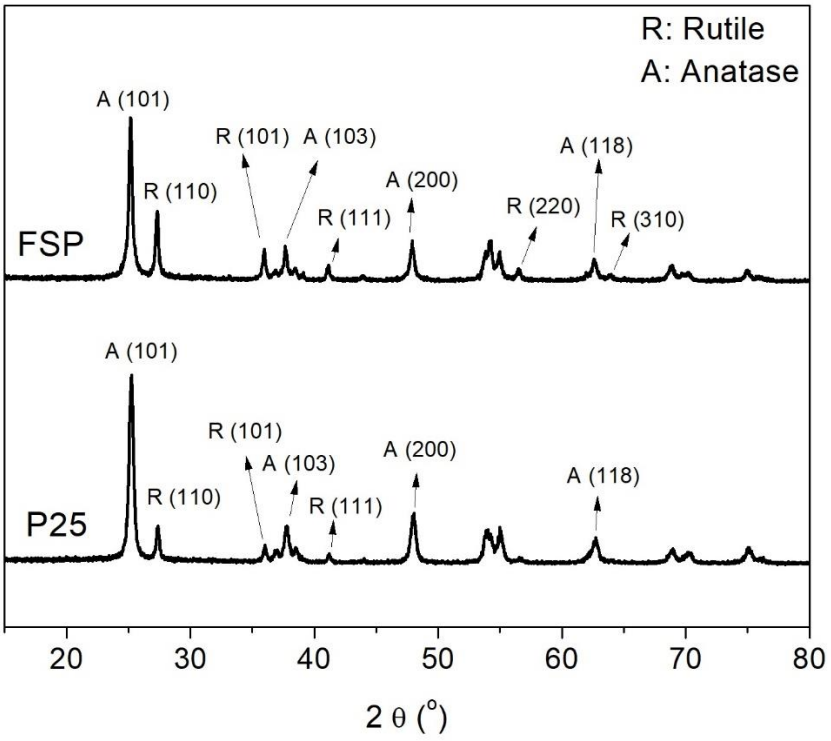

Figure 1: XRD patterns of FSP and P25 samples and related phase identification

Table 4: Properties of the samples derived from XRD, N_2 sorption isotherms at -196 ºC and Band gap calculation from DR UV-Vis data elaborated according to Tauc plots.

	P25					FSP				
Sample	**Bare**	**0.1%Pt**	**0.1%Pd**	**0.1%Ag**	**0.1%Au**	**Bare**	**0.1%Pt**	**0.1%Pd**	**0.1%Ag**	**0.1%Au**
Anatase/rutile(%)	78/22	87/13	81/19	87/13	87/13	65/35	64/36	64/36	70/30	70/30
Crystallite diameter (nm) [a]	15	21	20	21	21	23	33	22	30	28
BET surface area ($m^2 g^{-1}$) [b]	45	55	57	61	47	68	60	57	72	65
t-plot micropore volume ($cm^3 g^{-1}$) [c]	0.01	0.0036	0.0042	0.0040	0.0026	0.02	0.0037	0.00026	0.00043	0.0003
Total pore Volume ($cm^3 g^{-1}$)[d]	0.11	0.32	0.25	0.31	0.28	0.14	0.25	0.21	0.36	0.30
Band Gap energy (eV) [e]	3.4	3.1	3.2	3.2	3.3	3.3	3.1	3.0	3.2	3.1

[a] Particle size quantification from XRD data through the Scherrer equation.
[b] as calculated from N_2 adsorption/desorption isotherms, collected at -196 °C.
[c] as calculated by applying the t-plot method.
[d] as calculated from N_2 adsorption/desorption data at $p/p° = 0.97$
[e] as calculated by the Tauc equation from DR-UV-Vis spectra.

N_2 adsorption/desorption data were elaborated through the BET algorithm to get the specific surface area and microporous volume was calculated according to the t-plot method. The results are reported in Table 4.

Both P25 and FSP samples show a type II isotherm with H1 hysteresis loop, representing the agglomerates or spherical particles arranged uniformly with high pore size uniformity and facile pore connectivity (Figure 2) [53]. FSP samples, however, show higher surface area with respect to P25, which may positively affect its catalytic performance. Loading with co-catalysts, decrease the micropore volume, mainly due to partially blocking of the micropores by formation of new fragments coming from loading procedure and imposing distance between the particles in the crystalline structure.

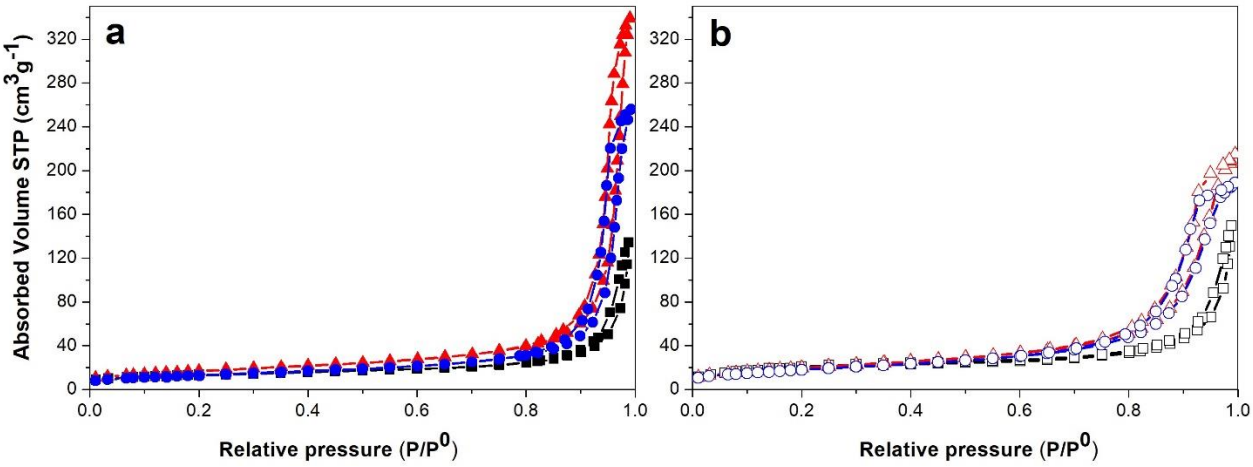

Figure 2: Example of N_2 adsorption/desorption isotherms collected at -196 ºC over three selected samples outgassed overnight at 150°C. a) P25 samples (full squares) 0.1% Au-P25 (full circles), 0.1% Ag-P25 (full triangles). b) FSP samples (hollow squares), 0.1% Au-P25 (hollow circles), 0.1% Ag-P25 (hollow triangles)

According to UV absorption spectra (Figure 3), both P25 and FSP samples show a strong absorption in the range of 240–380 nm, due to electron transfer from the 2p valence band (VB) orbital of O to the 3d conduction band (CB) orbital of Ti [54,55]. The UV absorption spectra shows the cut-off wavelengths of un-doped TiO_2 samples at shorter wavelengths with respect to bare P25 and FSP. The main reason for the bathochromic shift in transition and the visible light absorption is attributed to alteration of the energy levels of the semiconductor band gap and a charge transfer between the metal CB and the VB or the d–d transition in the crystal field [52].

The optical band gap energy E_g was calculated according to the Tauc equation (Table 4) [56]. Addition of metals to TiO_2 samples shifted the absorption edge to longer wavelengths and reduced the band gap [54,57].

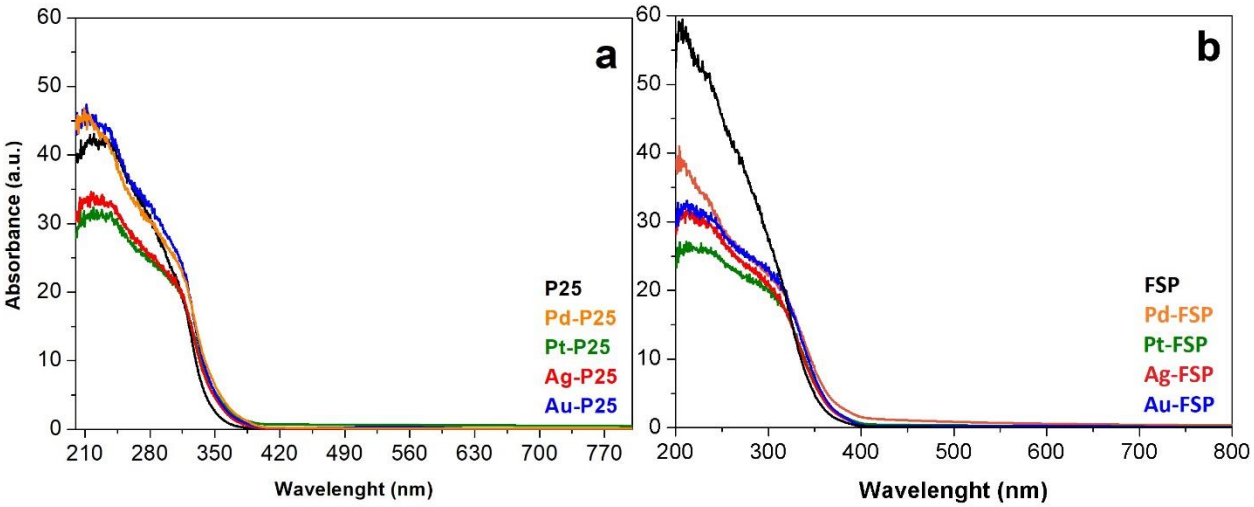

Figure 3: DR UV-Vis spectra of P25 (a) and FSP (b) samples.
Bare FSP and P25 titania (black curve); Pt co-catalyst (green curve); Pd co-catalyst (orange curve); Ag co-catalyst (red curve) and Au co-catalyst (blue curve)

3.2. Activity testing for the photoreduction of Nitrates

3.2.1 – Effect of pH

In order to find the optimum pH condition the photoreduction of nitrates has been performed at four different pH (2.5, 5.1, 9.2 and 11.5). Furthermore, the surface charge properties of P25 and FSP catalysts have been studied based on the electrophoretic mobility as a function of pH at 25 ˚C by electrophoretic light scattering technique and the point of zero charge (PZC) has been found based on ζ potential measurements. The variation of the pH of the solution changes the surface charge of TiO_2 particles and shifts the potentials of catalytic reactions. As a result, the adsorption of Nitrates on the surface may altered thereby causing a change in the reaction rate. Under acidic or alkaline condition, the surface of Titania can be protonated or deprotonated respectively according to the following reactions, the former species being predominant for pH < PZC and the latter for pH > PZC:

$$(eq\ 26) \qquad TiOH + H^+ \rightarrow TiOH_2{}^+$$

$$(eq\ 27) \qquad TiOH + OH^- \rightarrow TiO^- + H_2O$$

PZC was calculated as pH 6.25 and 4.5 for P25 and FSP, respectively (Figure 4).

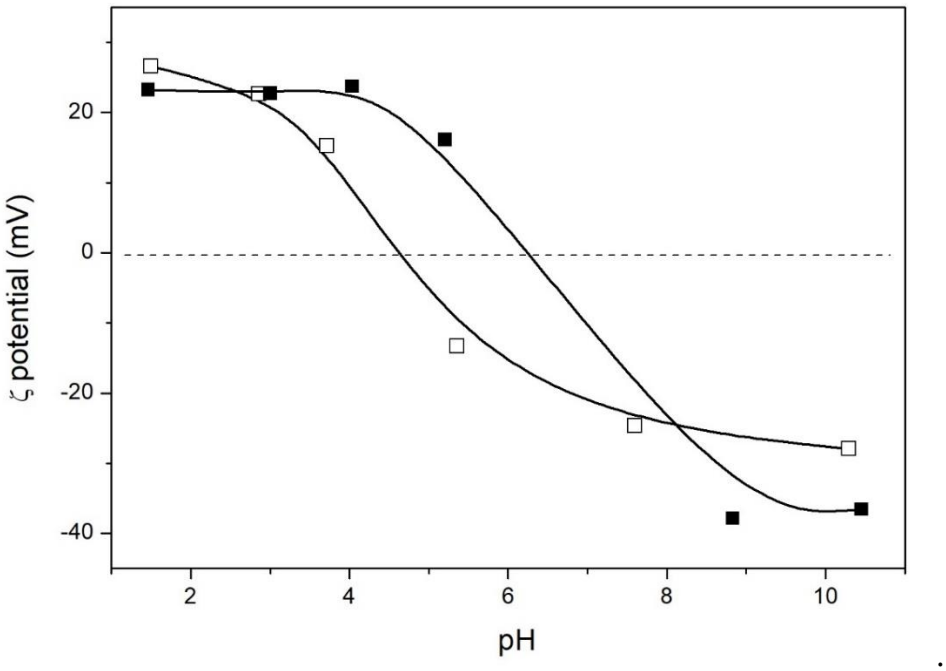

Figure 4: ζ-potential curves of P25 (full squares) and FSP (hollow squares)

The nitrates conversion is affected by the pH of the solution, since a positively charged surface would enhance the nitrate adsorption and viceversa. However, the electrostatic interaction between the catalyst surface and nitrate ions should not be rate limiting. Indeed, higher activity for FSP catalysts has been achieved at pH for which the catalysts has nearly neutral surface (Fig. 5b). On the other hand, for P25 higher activity achieved at basic pH in which catalyst surface was deprotonated and thus negatively charged, which would disfavor the adsorption of the reactant (Figure 5a). This means that the rate determining step of the reaction is not the surface adsorption. As for the selectivity, Ammonia was the only detected by-product, besides N_2, since nitrites did not accumulate significantly under the present conditions. Ammonia selectivity decreased for every catalyst when increasing the pH. A first explanation could be a stripping effect due to the semi-batch working conditions. However, significant stripping at basic pH was excluded on the basis of an extensive parallel investigation on the photo-oxidation of ammonia. In such a case,

even varying the initial ammonia concentrations we had no evidence of stripping. A zeolite trap was also placed downstream the reactor and periodically regenerated. The Temperature Programmed Desorption of the zeolite bed evidenced the desorption of water but negligible ammonia, at least using the gas flow and temperature of these tests.

3.2.1.1. The role of pH on formation of different intermediates

The pH dependence of NO_3^- photo-reduction is a controversial issue [58] most likely due to formation of many intermediate compounds in the process, such as peroxynitrous acid (ONOOH)/peroxynitrite ($ONOO^-$) (eq 9), (•NO) (eq 10), or nitrogen dioxide ($•NO_2$) (eq 8) [58–60]. However, the formation pathways of these substances are still under debate [58,61].

For P25 increasing the pH from acidic to basic increased the Nitrate conversion and decreased the ammonia selectivity (Figure 5a).

At pH ≤3.4, nitrite was an intermediate, apparently in the protonated form (pKa of HNO_2/NO_2^- is approximately 3.4), whereas ammonium was the main by-product (Eq. 12 and 18) [42]. Although in our experiments we did not observe any nitrogen-containing gaseous products except N_2, Park et al [45], explained the possible disproportionation of nitrous acid (HNO_2) to NO and NO_2 at this range of pH with a fast rate (Eq. (21), $k = 13.4 \times 10^8$ 1/M.s), which may be the key limitation for the further reduction toward N_2 or NH_4^+.

At $3.4 \leq pH \leq 5.1$, Nitrates conversion slightly increased, whereas ammonium selectivity decreased. At pH ≥ 6.8, nitrite was the only by-product which further reduced to N_2 gas (eq. 19) or back oxidized to nitrates consuming $OH^•$ (eq.22, 23 and 25).

Wagner et al. [62] and later Zhu et al. [41] proposed alternative hypotheses, which are in fare

agreement with our explanation. Based upon the kinetic trends found in this study and further literature information confirmed that $ONOO^-$ was the dominant photochemical product in the photolysis of NO_3^- (eq 9) (Goldstein and Czapski, 1997; Thøgersen et al., 2009) and the dominant channel for photo-decay of $ONOO^-$ is (eq 10) (Thøgersen et al., 2015). During the process, there are three possible reasons to explain the pH dependence on NO_2^- formation: i) at pH ≤ 6.8, ONOOH is a dominant by-product and it can be isomerized to NO_3^- rapidly (pKa of HNO_3/ $ONOO^-$ is 6.8), resulting in low photo-reduction rate [62], whereas at pH ≥ 6.8, $ONOO^-$ is a dominant byproduct and can lead to high photo-reduction rate; ii) $ONOO^-$ is an active scavenger for •OH, though precluding the oxidation of NO_2^- or $•NO_2$ by •OH at high pH [58,61]; iii) NO_2^-photolysis to NO_3^- by UV_{254nm} was slower at high pH than that at low pH.

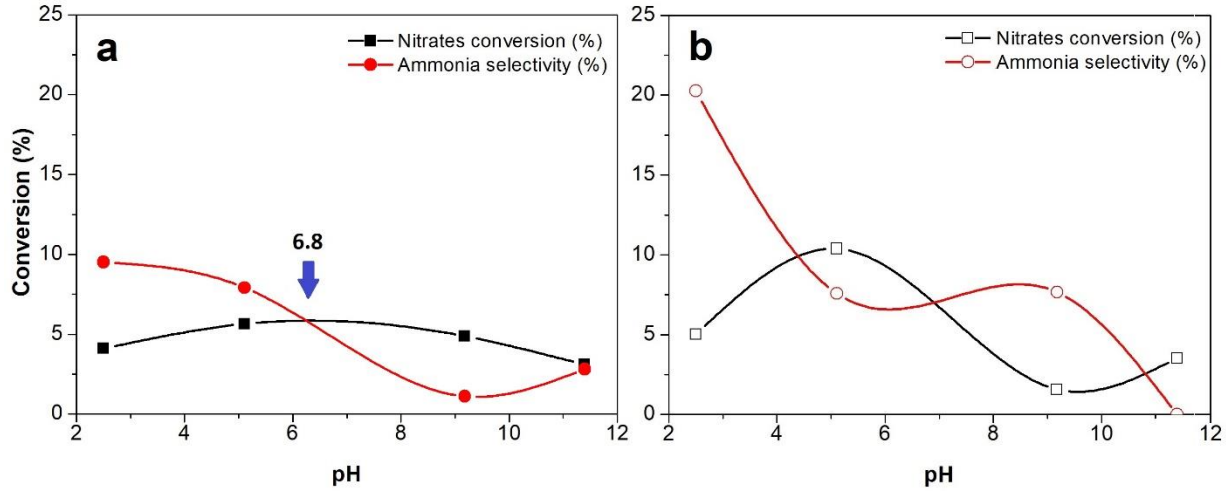

Figure 5: Nitrate conversion and ammonium selectivity (balance N_2) at different initial pH with a) P25 and b) FSP photocatalysts after 5 h reaction time.

Finally, it should be remembered that the same photocatalysts may promote the water reduction to H_2. Low pH means a high concentration of H^+, which can undergo reduction to H_2 by e_{CB}^-, competing with nitrates for reduction. H_2 is in principle detectable through GC, but due to very low concentration, the semibatch reactor configuration which prevents products accumulation in

gas phase and the very low sensitivity to H_2 of the TCD detector with He as carrier gas, it was not detected through the experiments. Therefore, the competing H_2 formation should be considered as a possible explanation of the low nitrate conversion achievable, especially at low pH.

3.2.1.2. The role of pH on semi-reduction potentials

pH directly affects the reduction potential of the different redox couples involved in the reaction. As said, at acid pH the high concentration of H^+ can favour hydrogen production that can compete with nitrates removal, whereas, at higher pH, higher concentration of OH^- and consequent formation of OH• is favoured.

The standard reduction potentials for Nitrate and hydrogen has been reported below:

$$(eq\ 16) \qquad NO_3^- + 6H^+ + 5e^- \rightarrow {}^1/_2\, N_2 + 3H_2O \qquad E^0(NO_3^-/N_2) = 1.25\ V$$

$$(eq\ 12) \qquad NO_3^- + 10H^+ + 8e^- \rightarrow NH_4^+ + 3H_2O \qquad E^0\left(NO_3^-/NH_4^+\right) = 0.88\ V$$

$$(eq\ 14) \qquad NO_3^- + 2H^+ + 2e^- \rightarrow NO_2^- + H_2O \qquad E^0(NO_3^-/NO_2^-) = 0.84\ V$$

$$(eq\ 4) \qquad 2H^+ + 2e^- \rightarrow H_2 \qquad E^0(H^+/H_2) = 0.0\ V$$

Half reaction potential depends directly on temperature, pressure and concentration of the species in solution. Consequently, varying the concentration of H^+, alters the reduction potentials of all the above reported reactions. Accordingly, the potentials are calculated through the Nernst equation:

$$(eq\ 28) \qquad E = E^0 + \frac{RT}{nF}\ln\frac{[ox]}{[red]}$$

Considering 25 °C, 1 atm and logarithmic change with (eq 28), (eq 16) can be rewritten as

$$(eq\ 29) \qquad E = E^0(NO_3^-/N_2) - \left(\frac{0.0591}{5}\right)\log\left(\frac{(p_{N2})^{\frac{1}{2}}}{[H^+]^6[NO_3^-]}\right)$$

Due to the continuous helium bubbling, calculating the concentrations at equilibrium condition is not feasible, however, calculations were performed assuming standard condition with unitary concentration of involved species (*e.g.* [N_2], [NO_3^-], [H^+]). Consequently, the same calculations were performed for all reactions:

$$(eq\ 30) \qquad E = E^0(NO_3^-/N_2) - 6\left(\frac{0.0591}{5}\right)pH$$

$$(eq\ 31) \qquad E = E^0\left(NO_3^-/NH_4^+\right) - 10\left(\frac{0.0591}{8}\right)pH$$

$$(eq\ 32) \qquad E = E^0(NO_3^-/NO_2^-) - 2\left(\frac{0.0591}{2}\right)pH$$

$$(eq\ 33) \qquad E = E^0(H^+/H_2) - 2\left(\frac{0.0591}{2}\right)pH$$

The calculated values of reduction potentials at different pH conditions of our experiments have been reported in Table 5.

Table 5: The reduction potential of different compounds

pH	$E(NO_3^-/N_2)$	$E(NO_3^-/NH_4^+)$	$E(NO_3^-/NO_2^-)$	$E(H^+/H_2)$
0.0	1.25	0.88	0.84	0
2.5	1.07	0.69	0.69	-0.14
5.1	0.88	0.50	0.54	-0.30
9.2	0.59	0.20	0.29	-0.54
11.5	0.43	0.03	0.16	-0.67

The CB and valance band (VB) of TiO_2 are respectively made up of Ti 3d and O 2p. The relationship between the electrode potential for conduction band minimum (CBM), valence band maximum (VBM) (EP_c, EP_v) and band gap energy (E_g) can be approximately expressed by the equations [63], valid as comparison with the Normal Hydrogen Electrode at pH=0.

$$(eq\ 34) \qquad EP_c\ (V\ vs. NHE) = 1.23 - E_g(ev)/2$$

$$(eq\ 35) \qquad EP_v\ (V\ vs. NHE) = 1.23 + E_g(ev)/2$$

The E_g for pure anatase TiO_2 is 3.2 eV, so the EP_c and EP_v are about –0.37 V (vs. NHE) and +2.83 V (vs. NHE), respectively. Since the the band gap of semiconductors is poorly affected by the pH and it is mainly depending on the crystalline structure [64], the new potentials in different pH based on the CBM and VBM of TiO_2 has been plotted in Figure 6, where the band positions reported in the literature have been reported only at pH = 0, based on literature data (eq. 34-35 [63]). Possibly, different bands bending at the surface may affect the resulting electron and hole potentials at the surface, but this deserves direct measurement for each case.

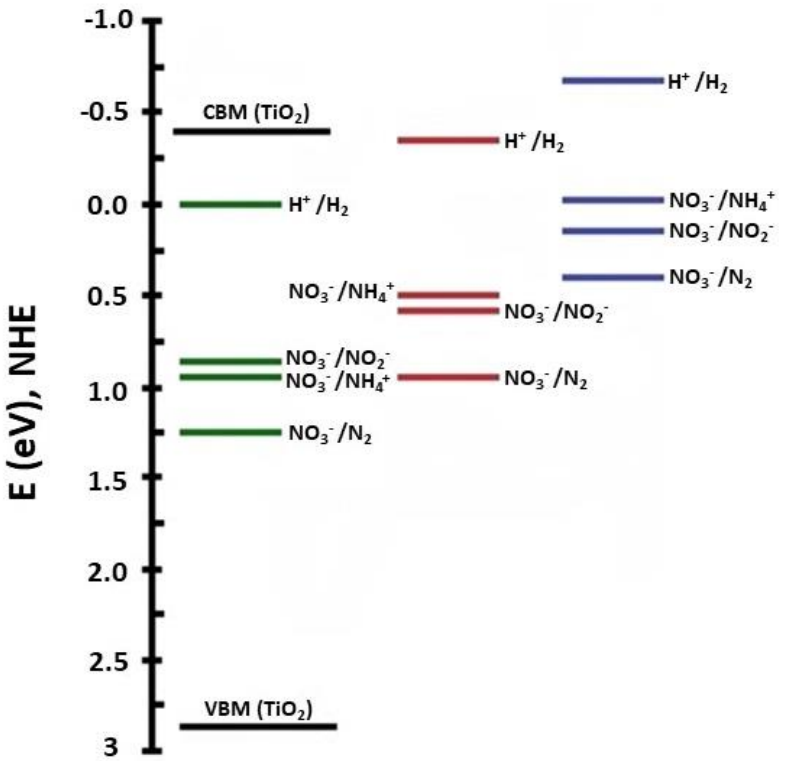

Figure 6: Half reaction potentials of the main reactions at different pH values. pH = 0 (green, left); pH = 5.1 (red, middle); pH = 11.5 (blue, right).

From this preliminary evaluation of half reduction potential of different reactions the following assumption was given. At pH 11.5 the half reaction potential for hydrogen formation is above the CBM of P25 titanium dioxide, therefore, this reaction is no longer possible to compete with

reduction of Nitrates. Consequently, we observed a high nitrate conversion at corresponding pH. This explanation is in a fair agreement with the recent study of Challagulla et al., (2017) [65] on the effect of pH on half reaction potential in the photocatalytic reactions. On the other hand, considering the nitrate conversion for the other three pH values, hydrogen formation has negative impact on nitrate reduction. However, the best conversion was obtained at pH 5.13 in which the surface of P25 is positively charged and a possible electrostatic attraction with nitrates could explain this result. At lower pH (*e.g.* 2.5), higher [H^+] favours the hydrogen production.

The FSP catalyst follows the same trend as P25 however, the maximum nitrate conversion has been obtained at pH 5.1 with neutrally charged surface (Figure 5b). The maximum nitrate conversion after 5h of reaction was slightly higher for the FSP catalyst (10.4 % conversion) with respect to P25 (9 % conversion).

The higher nitrates conversion for the FSP can be justified by its higher surface area (67 vs. 45 m^2/g) and lower bang gap (3.31 vs 3.41 eV) with respect to P25. Furthermore, higher concentration of anatase and rutile (anatase: 65% and rutile: 35%) interface boundary exists for FSP, which can favor the charge separation across the interface of the two phases. Last but not the least, the flame spray pyrolysis technique, imposes more crystalline defects in the structure of nanoparticles with typically fully oxidized and highly crystalline morphology, due to the abundance of oxygen and high temperature in the synthesis procedure [28,48,49,66]. The surface defects are advantageous for catalytic and photocatalytic reactions, since these are the surface energetic facets with minimal charge recombination centers and electron-hole pair charge trapping (deep traps) [67].

At pH 5.1 nitrates adsorption is favored on the nearly neutral surface of the FSP catalyst, which may be one of the factors for demonstrating the maximum conversion. Furthermore, since the surface is not charged, the catalyst may be a more efficient charge trap, due to lower density of

charge in this pH range. By increasing the pH, the bulk electron diffusion increases and the photoelectrons that are shallowly or deeply trapped at these sites [67], tend to have faster recombination with holes and therefore the nitrate conversion at this pH was lower with respect to the P25 catalyst. Another explanation may be the higher negative charge density of FSP at basic pH with respect to P25 due to the higher density of crystalline defects, which may result in stronger electrostatic repulsion between the negative catalyst surface and the negative nitrate ions and therefore, lower photocatalytic activity at this pH.

3.2.2 - Effect of co-catalyst

The results of photoreduction tests with P25, FSP and their co-catalysts at the optimum pH previously determined are plotted in Figure 7 and summarized in Table 6.

According to results, the addition of a co-catalysts was not determinant to increase the photoreduction activity. Also, noble metals improve the competitive conversion of protons to hydrogen and therefore the CB electrons of the supporting semiconductor are not available for nitrate reduction [40,68]. Although as said our experiments have been performed in semi batch mode and no H_2 production has been quantified, the results of nitrates conversion are in a fare agreement with Callangula et al. [65].

According to nitrate conversion after 5 hours of reaction (Figure 7a), the photoreduction of nitrate over Pd-P25, Pt-P25 and Au-P25 was slower than for the bare catalyst. Ag-P25 showed the best performance over other noble metals, nonetheless with poorer overall performance with respect to bare P25 due to its higher selectivity toward ammonia.

Challagulla et al. [65] claimed the higher activity of metals, such as Pt and Pd with respect to Ag and Au for the production of hydrogen rather than nitrate reduction.

Considering the co-catalysts active for nitrates reduction with plasmonics effect, silver shows better activity over Au. There are two possible explanation for this behavior: a) Silver can support surface plasmons (SPs) in the visible (Vis) and near-infrared regions (NIR) of the spectrum from 300 to 1200 nm, whereas, for Au, the SPR excitations is limited for wavelengths longer than 500 nm [69]; b) The location of sub-bands of Ag and Au with respect to conduction band (CB) of titania are favoring different mechanisms, following different photocatalytic activity. Accordingly, the location of sub-bands of Ag is far from conduction band (CB), therefore, photoexcited electrons tend to be more available for nitrate reduction, whereas, in the presence of gold, the excited electron in the CB of TiO_2 might be redistributed to the plasmonic domains of gold rather than be available for nitrates reduction [65].

These observations confirm that the photogenerated electrons are the main species that are responsible for the nitrate reduction.

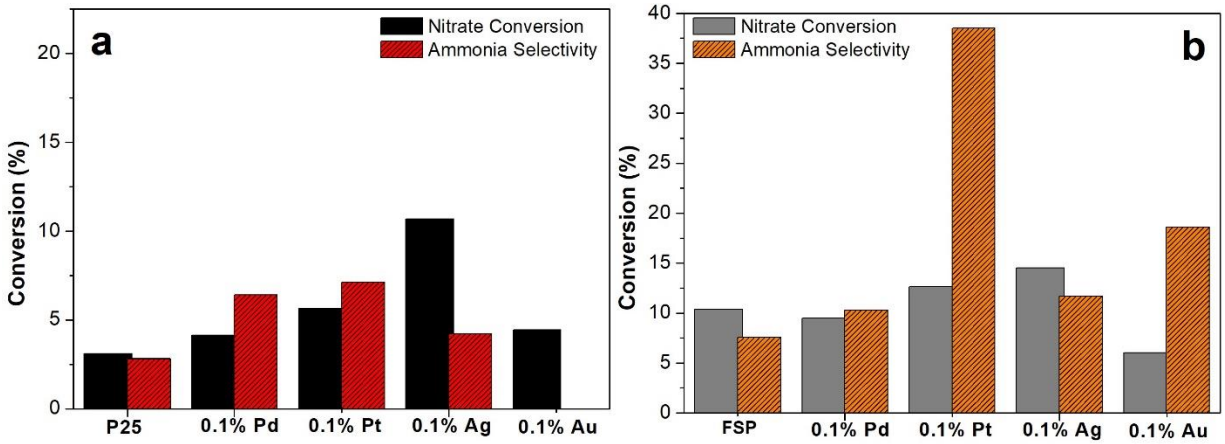

Figure 7: Nitrate conversion and ammonia selectivity after 5h of irradiation with different co-catalyst on (a) P25 at pH 11.5 and (b) FSP at pH 5.1.

For FSP titania samples, the selectivity toward ammonia increased with co-catalysts addition, together with conversion, likely due to better charge separation (Figure 7b). Although, for nitrate reduction the main difference between FSP titania and P25 one is the conversion ratio among bare

catalyst and Pt, Pd doped samples. This behavior may relate to the physical property of the catalysts as discussed before such as punctual defects that can help charge separation.

Table 6: Photocatalytic activity of different catalysts for nitrate reduction (1 g/L catalyst except for test number 70 1.25 g/L).

TiO_2 (Test #)	Co-cat (mol%)	pH	NO_3^- Conc (mM)	Catalyst (g/L)	Max NO_3^- conv% (time of max conversion, h)	Rate (mmol/ h g_{cat})	Sel. NH_4^+ (%)
P25 (70)	-	11.5	6	1.25	3.09 (5)	0.030	2.81 (5)
P25 (71)	0.1 Pd	11.5	6	1	4.86 (3)	0.050	14.73 (3)
P25 (74)	0.1 Au	11.5	6	1	4.40 (4)	0.050	0 (5) 9.0 (2)
P25 (73)	0.1 Ag	11.5	6	1	10.67 (5)	0.125	4.21 (5)
P25 (75)	0.1 Pt	11.5	6	1	5.66 (5)	0.062	6.4 (5)
FSP (65)	-	5.1	6	1	10.38 (5)	0.125	7.57 (5)
FSP (87)	0.1 Pd	5.11	6	1	9.80 (4)	0.125	10.35 (5)
FSP (85)	0.1 Au	5.11	6	1	6.02 (4)	0.075	18.60 (5)
FSP (88)	0.1 Ag	5.11	6	1	14.50 (5)	0.175	11.7 (5) 62 (1)
FSP (86)	0.1 Pt	5.11	6	1	12.60 (5)	0.162	38.5 (5) 81 (2)

4. Conclusions

This work has been focused on the pH study and effect of four different noble metal co-catalysts for P25 and FSP titanium dioxide in the nitrate photoreduction. The optimal pH values was 11.4 and 5.1, with nitrate conversion after 5 h reaction time of 8.8% and 10.4% for P25 and FSP, respectively.

Formation of different intermediates due to pH change, may favor different mechanisms, favoring or disfavoring the nitrate reduction. In general, ammonia selectivity increased at acidic pH, whereas at basic pH its selectivity was much lower.

Adding noble metals as co-catalyst improved in general the reduction activity of the catalyst, possibly favouring competitive reactions and most of all increasing the selectivity toward ammonia formation. Ag showed the best performance for both FSP and P25 samples with 14.5% and 10.7% conversion in 5h of reaction time, respectively, but also in this case the conversion/selectivity dependence should be carefully considered.

ACKNOWLEDGEMENTS

The financial support of Fondazione Cariplo through the measure “Ricerca sull’inquinamento dell’acqua e per una corretta gestione idrica”, grant no. 2015-0186, is gratefully acknowledged.

References

[1] D. A. Bronk, in (Eds.: D.A. Hansell, C.A. Carlson), Elsevier, New York, **2002**, pp. 153–247.

[2] B. . Rosenstock, M. Simon, *Limnol. Ocean.* **1993**, *38*, 1521–1531.

[3] C. A. Martinez-Huitle, E. Brillas, *Appl. Catal. B Env.* **2009**, *87*, 105–145.

[4] U. von Gunten, *Water Sci. Technol* **2007**, *55*, 25–29.

[5] P. M. Vitousek, J. D. Aber, R. W. Howarth, G. E. Likens, P. A. Matson, W. H. Schindler, D.W. Schlesinger, D. G. Tilman, *Ecol. Appl* **1997**, *7*, 737–750.

[6] S. S. Perakis, L. O. Hedlin, *Nature* **2002**, *415*, 416–419.

[7] R. Hirsch, T. A. Ternes, K. Haberer, K. L. Kratz, *Vom Wasser* **1996**, *87*, 263–274.

[8] J. S. Jensen, G. R. Hetz, *Environ. Sci. Technol.* **1998**, *32*, 516–522.

[9] OECD, *Environmental Outlook to 2030*, OECD Publishing, **2008**.

[10] C. C. A. Loures, M. A. K. Alcântara, H. J. I. Filho, A. A. C. Teixeira, F. T. Silva, T. C. B. Paiva, G. R. L. Samanamud, *Int. Rev. Chem. Engin* **2013**, *5*, 102–120.

[11] M. Klavarioti, D. Mantzavinos, D. Kassinos, *Env. Int* **2009**, *35*, 402–417.

[12] T. Robinson, G. McMullan, R. Marchant, P. Nigam, *Bioresour. Technol.* **2001**, *77*, 247–255.

[13] K. Grohmann, E. Gilbert, S. H. Eberie, *Acta Hydrochem. Hydrobiol* **1998**, *26*, 20–30.

[14] S. D. Richardson, M. J. Plewa, E. D. Wagner, R. Schoeny, D. M. DeMarini, *Mutat. Res* **2007**, *636*, 178–242.

[15] W. H. Glaze, J.-W. Kang, D. H. Chapin, *Ozone Sci. Eng.* **1987**, *9*, 335–352.

[16] I. Oller, S. Malato, J. A. Sánchez-Pérez, *Sci. Total Env.* **2011**, *409*, 4141–4166.

[17] S. C. Ameta, in *Adv. Oxid. Process. Waste Water Treat.* (Eds.: S.C. Ameta, R. Ameta), Elsevier, **2018**, p. 428.

[18] M. Compagnoni, G. Ramis, F. S. Freyria, M. Armandi, B. Bonelli, I. Rossetti, *J. Nanosci. Nanotechnol.* **2017**, *17*, 1–22.

[19] I. Rossetti, M. Compagnoni, G. Ramis, F. Freyria, M. Armandi, B. Bonelli, *Chem. Eng. Trans.* **2017**, *57*, 2283–9216.

[20] M. Compagnoni, G. Ramis, F. S. Freyria, M. Armandi, B. Bonelli, I. Rossetti, *Rend. Lincei* **2017**, *28*, 151–158.

[21] I. Rossetti, E. Bahadori, A. Tripodi, G. Ramis, *DGMK-Tagungsbericht 2018-2, ISBN 978-3-941721-87-6* **2018**, 147–154.

[22] M. N. Chong, B. Jin, C. W. Chow, C. Saint, *Water Res* **2010**, *44*, 2997–3027.

[23] E. Bahadori, M. Compagnoni, A. Tripodi, F. Freyria, M. Armandi, B. Bonelli, G. Ramis, I. Rossetti, *Mater. Today Proc.* **2018**, *5*, 17404–17413.

[24] F. S. Freyria, M. Armandi, M. Compagnoni, G. Ramis, I. Rossetti, B. Bonelli, *J. Nanosci. Nanotechnol.* **2017**, *17*, 3654–3672.

[25] S. Malato, J. Blanco, J. Cáceres, A. R. Fernández-Alba, A. Agüera, A. Rodríguez, *Catal. Today* **2002**, *76*, 209–220.

[26] M. J. Watts, A. T. Cooper, *Sol. Energy* **2008**, *82*, 206–211.

[27] I. K. Konstantinou, T. A. Albanis, *App. Catal. B-Environ* **2004**, *29*, 1–14.

[28] L. Giacomo, B. Maria, V. Diamanti, M. Sansotera, M. Pia, P. Walter, N. Paolo, *J. Nanoparticle Res.* **2016**, *18*, 238.

[29] G. L. Chiarello, I. Rossetti, P. Lopinto, G. Migliavacca, L. Forni, *Catal. Today* **2006**, *117*, 549–553.

[30] L. Biyoghe Bi Ndong, M. P. Ibondou, X. Gu, S. Lu, Z. Qiu, Q. Sui, S. Maurice Mbadinga, *Ind. Eng. Chem. Res.* **2014**, *53*, 1368–1376.

[31] Y.-H. Chen, M. Franzreb, R.-H. Lin, L.-L. Chen, C.-Y. Chang, Y.-H. Yu, P. Chi Chiang, *Ind. Eng. Chem. Res.* **2009**, *48*, 7616–7623.

[32] C. González, M. Bartoszek, A. Martin, C. . Correa, *Ind. Eng. Chem. Res.* **2009**, *48*, 2826–2835.

[33] D. Ma, Y. Yan, H. Ji, C. Chen, J. Zhao, *Chem. Commun.* **2015**, *51*, 17451–1754.

[34] C. F. Bohren, D. R. Huffman, *Absorption and Scattering of Light by Small Particles*, Wiley, New York, **1983**.

[35] U. Kreibig, M. Vollmer, in (Ed.: M. Vollmer), Springer, Berlin, **1995**.

[36] B. Nikoobakht, M. A. El-Sayed, *Chem. Mater* **2003**, *15*, 1957−1962.

[37] J. Pérez-Juste, I. Pastoriza-Santos, L. M. Liz-Marzán, P. Mulvaney, *Coord. Chem. Rev.* **2005**, *249*, 1870−1901.

[38] J. Jing, M. Liu, V. L. Colvin, W. Li, W. W. Yu, *J. Mol. Catal. A Chem.* **2011**, *351*, 17–28.

[39] M.-S. Kim, S.-H. Chung, C.-J. Yoo, M. . Lee, I.-H. Cho, D.-W. Lee, K.-Y. Lee, *Appl. Catal. B, Environ.* **2013**, *142*, 354–361.

[40] M. Shand, J. a. Anderson, *Catal. Sci. Technol.* **2013**, *3*, 879–899.

[41] J. Wang, M. Song, B. Chen, L. Wang, R. Zhu, *Chemosphere* **2017**, *184*, 1003–1011.

[42] K. Doudrick, T. Yang, K. Hristovski, P. Westerhoff, *Appl. Catal. B Env.* **2013**, *136–137*, 40–47.

[43] J. A. Frank, M. Gratzel, *Inorg. Chem* **1982**, *21*, 3834–3837.

[44] Y. Li, W. Wang, Z. Zhan, M. Woo, C. Wu, P. Biswas, *Appl. Catal. B, Environ.* **2010**, *100*, 386–392.

[45] J. Y. Park, Y. N. Lee, *J. Phys. Chem.* **1988**, *92*, 6294–6302.

[46] G. Barker, P. Fowles, B. Stringer, *Trans. Faraday Soc* **1970**, *66*, 1509–1519.

[47] P. Maurer, C. F. Thomas, R. Kissner, H. Rüegger, O. Greter, U. Rothlisberger, W. H. Koppenol, *J. Phys. Chem* **2003**, *107*, 1763–1769.

[48] M. Compagnoni, J. Lasso, A. Di Michele, I. Rossetti, *Catal. Sci. Technol.* **2016**, *6*, 6247–6256.

[49] G. L. Chiarello, I. Rossetti, L. Forni, *J. Catal.* **2005**, *236*, 251–261.

[50] K. Thamaphat, P. Limsuwan, B. Ngotawornchai, *Kasetsart J. (Nat. Sci.)* **2008**, *361*, 357–361.

[51] R. A. Spurr, H. Myers, *Anal. Chem.* **1957**, *29*, 760–762.

[52] R. Chauhan, A. Kumar, R. P. Chaudhary, *Res. Chem. Intermed.* **2012**, *38*, 1443–1453.

[53] M. Thommes, K. Kaneko, A. V Neimark, J. P. Olivier, F. Rodriguez-reinoso, J. Rouquerol, K. S. W.

Sing, in *Pure Appl. Chem.* (Eds.: H. Burrows, J. Stohner), The Scientific Journal Of IUPAC, **2015**, pp. 1051–1069.

[54] N. Seifvand, E. Kowsari, *Ind. Eng. Chem. Res.* **2016**, *55*, 10533–10543.

[55] S. Tan, B. . Chen, W. Sun, X, W. J. Fan, H. S. Kwok, X. H. Zhang, *J. Appl. Phys* **2005**, *98*, 013505.1-013505.5.

[56] P. Li, H. Hu, J. Xu, H. Jing, H. Peng, J. Lu, *Appl. Catal., B Env.* **2014**, *147*, 912–919.

[57] S. I. Mogal, V. G. Gandhi, M. Mishra, S. Tripathi, T. Shripathi, P. . Joshi, D. O. shah, *Ind. Eng. Chem. Res.* **2014**, *53*, 5749–5758.

[58] J. Mack, J. R. Bolton, *J. Photochem. Photobiol. A Chem* **1999**, *128*, 1–13.

[59] G. Mark, H.-G. Korth, H.-P. Schuchmann, C. von Sonntag, *J. Photochem. Photobiol. A Chem* **1996**, *101*, 89–103.

[60] N. Lu, N.-Y. Gao, Y. Deng, Q.-S. Li, *Water Sci. Technol* **2009**, *60*, 1393–1400.

[61] C. M. Sharpless, K. G. Linden, *Environ. Sci. Technol* **2001**, *35*, 2949–2955.

[62] I. Wagner, H. Strehlow, G. Busse, *Z Phys. Chem* **1980**, *123*, 1–33.

[63] Y. Matsumoto, *J. Solid State Chem.* **1996**, *126*, 227–234.

[64] O. Carp, C. L. Huisman, A. Reller, *Prog. Solid State Chem.* **2004**, *32*, 33–177.

[65] S. Challagulla, K. Tarafder, R. Ganesan, *J. Phys. Chem. C* **2017**, *121*, 27406–27416.

[66] W. Y. Teoh, *Mater.* **2013**, *6*, 3194–3212.

[67] G. Tsekuoras, M. Miyashita, Y. K. Kho, W. Y. Teoh, A. J. Mozer, R. Amal, S. Mori, G. G. Wallace, *IEEE J. Sel. Top. Quantum Electron* **2010**, *16*, 1641–1648.

[68] J. A. Anderson, *Catal. Today* **2011**, *175*, 316−321.

[69] M. Rycenga, C. M. Cobley, J. Zeng, W. Li, C. H. Moran, Q. Zhang, D. Qin, Y. Xia, *Chem. Rev.* **2011**, *111*, 3669–3712.

TOC

Photocatalysis has been used to reduce nitrate ions from waste and drinking water. A semibatch photoreactor was developed for this process and commercial nanostructured TiO_2 (P25) and TiO_2 in nanosized form prepared by flame spray pyrolysis (FSP) were used as catalysts, using several noble metals as co-catalysts. The bare and metal-promoted FSP samples, with higher surface area, showed higher nitrates conversion with respect to P25-based samples.